"The effects of immobilized carboxylic-functional groups on the dynamics of phase transformation from amorphous to octacalcium phosphate"

Yuki Sugiura[1,2], Kazuo Onuma[2], Masahiro Nagao[1] and Atsushi Yamazaki[1]*

1: Department of Resources and Environmental Engineering, School of Creative Science and Engineering, Waseda University, 3-1-4, Okubo, Shinjuku, Tokyo, 186-0049 Japan

2: National Institute of Advanced Industrial Science and Technology, Central 6, 1-1-1, Higashi, Tsukuba, Ibaraki, 305-8566 Japan

Corresponding author*

Dr. Kazuo Onuma

E-mail: k.onuma@aist.go.jp

FAX: +81-29-861-6149

Abstract

The influence of carboxylic-functional-groups (-COOH) on the phase transformation from amorphous calcium phosphate (ACP) to octacalcium phosphate (OCP) was investigated. 11-Mercaptoundecanoic acid, a carboxylic thiol, was immobilized on gold nanoparticles via covalent bond formation. Time-resolved static light scattering measurements indicated that a structural-reconstruction-type phase transformation occurred with or without the presence of -COOH on the nanoparticles. When it dispersed in calcium phosphate solutions, these nanoparticles inhibited the phase transformation dynamics and also changed the reaction path, forming HPO_4-OH-layer-deficient OCP at pH 6.5 an intermediate phase, which did not show the typical OCP X-ray diffraction (XRD) peak at $2\theta = 4.7°$. This phase was not observed in the reference solution containing gold nanoparticles without bound -COOH. The HPO_4-OH-layer-deficient OCP transformed to conventional OCP gradually, as revealed by XRD, nuclear magnetic resonance, and Raman analyses. Thus, the immobilized -COOH appeared to behave as a negative catalyst, resulting in the formation of the intermediate phase. Such a mechanism partially clarifies complex biomineralization processes, for example teeth enamel and dentin formation, *in vivo*.

KEYWORDS: biomineralization, calcium phosphate, phase transformation, early tooth formation, intermediate phase

INTRODUCTION

Biological organisms can construct complex functional hybrid structures from inorganic minerals and organic materials, such as nacres and bones (Mann 2001; Sunagawa 2005; Weiner and Dove 2003). During formation of these organs, organic molecules, polypeptides, and proteins act as templates for mineral nucleation and growth (Nudelman et al. 2013; Sunagawa 2005; Veis 2003), by providing preferential sites for mineral nucleation and control of the orientation of the precipitated crystals (Hamm et al. 2014). Some organic functional groups, such as -COOH, interact with Ca ions (Addadi et al. 2003; Gebauer et al. 2008; Falini et al. 1996). These groups greatly influence the nucleation and growth of Ca-containing minerals, particularly during amorphous phase formation (Addadi et al. 2003; Gebauer et al. 2008; Falini et al. 1996).

Tooth enamel is the hardest material in vertebrates (Nylen et al. 1963; Sunagawa 2005). It comprises highly organized hydroxyapatite (HAP) crystals elongated along their *c*-axis with a ribbon-like morphology. This structure is a proposed pseudomorph of octacalcium phosphate (OCP), (Brown et al. 1962; Iijima et al. 1992; Nelson et al. 1989; Wang and Nancollas 2008) which contains very few matrix proteins (Sunagawa 2005). When a tooth forms, HAP mineralization is aided by numerous organic molecules, whose roles have been investigated extensively. HAP mineralization is

accelerated by polypeptides rich in -COOH such as dentin matrix protein (He et al. 2003). Tsuji et al. 2008 also showed that soluble artificial proteins rich in -COOH accelerate the phase transformation from amorphous calcium phosphate (ACP) to HAP. Furthermore, self-assembled organic monolayers with terminal -COOH can form on noble metal substrates and facilitate nucleation of calcium phosphate (CP) in pseudo-physiological solutions (Dey et al. 2010; Nonoyama et al. 2011). Among the –COOH containing materials, citrate is known to have a definitive effect on the formation of HAP (Delgado-Lopez et al. 2012, 2014; Hu et al. 2010; Xie and Nancollas 2010).

However, the role of carboxylic rich materials in HAP precursor mineralization processes, such as those for OCP, remained unclear until a recent investigation indicated that they can alter the OCP structure through the modification of the HPO_4-OH layer (Davies et al. 2014). To the best of our knowledge, there have been few studies on the phases of ACP–OCP transformation in the presence of organic materials rich in -COOH, despite the fact that this transformation is essential in the early stages of tooth enamel formation (Zhao et al. 2012). In this study, immobilized -COOH were prepared using 11-Mercaptoundecanoic acid (MUA: $HS(CH_2)_{10}COOH$). The sulfur atoms of MUA covalently bind with gold atoms, forming a self-assembled carboxyl-terminated MUA

monolayer on the crystalline gold surface. These modified nanoparticles are referred to as **C**arboxylic-functional group on **G**old **N**anoparticle**s** (CGNs). To observe the effect of immobilized -COOH on the dynamics of ACP–OCP phase transformation, CGNs were dispersed in CP solutions. The phase transformation and resultant materials were investigated using several techniques, as described below.

MATERIALS AND METHODS

Preparation of the solutions used for ACP–OCP phase transformation studies.

$CaCl_2$ was purchased from Wako Pure Chemicals Inc., Japan, while KH_2PO_4, K_2HPO_4, and NaCl were purchased from Nakalai Tesque Inc., Japan. All the reagents were dissolved in ultra-pure water with a specific resistance of 18.2 MΩ. Three stock solutions were prepared: 1 M $CaCl_2$, 0.5 M KH_2PO_4, and 0.5 M K_2HPO_4. The KH_2PO_4 and K_2HPO_4 solutions were mixed together to obtain a 0.5 M phosphate solution (KDP–KAP) with a pH of 6.5. The final solution was prepared by mixing the KDP–KAP solution with $CaCl_2$ suspension, such that both Ca^{2+} and phosphate concentrations were 5 mM (pH 6.5 ± 0.1 at 22 °C). Because the volume ratio of the $CaCl_2$ suspension to the phosphate solution was less than 1: 100, the solution pH

reminded constant throughout the mixing process. All solutions were filtered using a 0.22 μm syringe-type membrane filter or a 0.22 μm centrifuge filter to remove dust particles before use.

Preparation and characterization of the -COOH immobilized on gold nanoparticles (CGNs).

The gold nanoparticles were a commercial-grade gold colloid (Gold Colloid 5 nm, BBI Solutions Co., UK), which contained approximately 300 μM gold. This solution (5 mL) was added to a 20 mM MUA (Sigma-Aldrich Japan K.K., Tokyo, Japan) ethanolic solution (5 mL) and the mixture was left at room temperature for more than 3 h to allow the formation of self-assembled MUA layers on the gold particles in a glass bottle. The solution was then dialyzed for more than 120 h in 3 L ultra-pure water through a cellophane membrane. The water was changed at 12 h intervals. The pH of the final solution containing CGNs was ~4.5. For comparison, a reference colloid solution containing non-immobilized gold nanoparticles was also dialyzed in ultra-pure water.

The CGNs were characterized using dynamic light scattering (DLS), zeta potential analysis and visible-light absorption spectroscopy.

In custom made multi-angle DLS systems (Kanzaki et al. 2006), to determine the angular dependence, the second autocorrelation functions $G^2(q, t)$ were simultaneously measured at scattering angles ranging from 30° to 100° (with 10° steps). The equipment light source was a semiconductor laser with a wavelength (λ_w) of 530 nm. The second autocorrelation functions $G^2(q, t)$ are expressed as follows:

$$G^2(q, t) = <I(q, t) \cdot I(q, 0)>/<I(q, t)>^2 + 1, \quad (1)$$

where $I(q, 0)$ and $I(q, t)$ are the scattered intensities at time zero and time t, respectively. The scattering vector q is a function of λ_w, the scattering angle θ, and the refractive index of the solution n.

$$q = 4\pi n \sin(\theta/2)/ \lambda_w \quad (2)$$

The decay time τ of the scattered particles was calculated from the $G^2(q, t)$ data using the CONTIN (Provencher 1982) program (ALV-Laser Vetriebsgesellschaft, ALV Co., Germany). For calculating τ, a number-weight analysis, instead of an intensity-weight analysis, was adopted because of the polydispersity of the reference gold nanoparticle and CGNs sizes, as determined via transmission electron microscopy (TEM) observation. The parameter τ is expressed in terms of q and the diffusion coefficient D of the scattered particles.

$$1/\tau = q^2 D \quad (3)$$

Because D is affected by intermolecular interactions between the particles, the relationship between D and the particle concentration was determined, and the translational diffusion coefficient D_0 was then estimated by extrapolating D at zero concentration.

D_0 can be converted to the hydrodynamic radius of particles r_H using the Stokes–Einstein equation.

$$r_H = k_B T/6\pi\eta D_0, \quad (4)$$

where η is the viscosity of water (η = 0.953 cP at 22°C).

Zeta-potential measurements revealed the presence of a double electric layer of colloidal particles in the solutions. The surface charge of the CGNs was compared with that of the dialyzed gold nanoparticles (reference) to estimate the formation of Au-S bonds on the gold nanoparticle surface using an ELSZ-1000Z photoelectric spectrometer (Otsuka Electric Co., Osaka, Japan). The particle concentration of the measured solutions was 50 μM. The solution temperature and pH were 25 °C and 6.5 (buffered using 5 mM KDP-KAP), respectively. A 30 mV semiconductor laser (λ_w=660 nm) was used as the light source, and the impressed voltage between the electrodes was 10 kV. The detection angle of the scattered light was 15° with an avalanche photodiode detector.

The formation of Au-S bonds on the gold nanoparticle surface was also estimated using visible-light absorption spectroscopy. The concentrations of the reference gold nanoparticle solution and CGNs-containing solution used for the measurements were both adjusted to 150 μM. The solutions were placed into a 4 mL square quartz cells and mounted on the spectrometer (V-630, Jasco Co., Hachioji, Japan). The absorption of H_2O was used for baseline calibration, and a deuterium lamp was used as the light source. The measured λ_w range was 500–800 nm with a scan rate of 50 nm/min.

Observation of the ACP–OCP phase transformation dynamics in solutions containing reference gold nanoparticles and CGNs using time resolved static light scattering (TR-SLS) and *in situ* Fourier transfer infrared spectroscopy (*in situ* FT-IR).

The theory and application of TR-SLS as well as the details of the optical instrument are described by Onuma et al. 2000. The main components of the instrument are an ellipsoidal mirror and a high-speed charge-coupled-device (CCD) camera. Using TR-SLS, the scattering intensity of the dispersed particles at scattering angles in the range 10°-170° can be obtained with an angle resolution of 1° and a maximum time resolution of 1 s. In this study, the interval was set to 2 s for each solution. The

181 measurement temperature of 22 °C was the same as that used for the DLS analyses, and
182 the light source was a He–Ne laser (λ_w = 632.8 nm).

183 Two types of reaction solutions were prepared for the TR-SLS analyses: a cationic
184 solution (1 M $CaCl_2$) and an anionic solution (5.03 M KH_2PO_4–K_2HPO_4 buffered at pH
185 6.5 with 10.01 μM reference gold nanoparticles or 10.01 μM CGNs). The cationic
186 solution (60 μL) was added to the anionic solution (11.94 mL), and the two solutions
187 were quickly mixed in the measurement cells. The final solution contained 5 mM Ca
188 and phosphate and 10 μM reference gold nanoparticles or CGNs. After solution
189 preparation, the changes in the molecular mass M_w and the gyration radius R_g of the
190 particles were measured.

191 In addition, the relationship between the scattering intensity and scattering angle
192 for each solution was analyzed using Zimm-square-root plots as follows.

193 The excess Rayleigh ratio ΔR of a sample solution (the difference in the scattering
194 intensity between the sample and buffer solution) depends on q, M_w, R_g, the particle
195 concentration c, the second virial coefficient of the particles A_2, and the optical constant
196 K, which includes the increase in the refractive index of the sample solution with
197 increasing particle concentration. The Rayleigh ratio is given by,

198 $$(Kc/\Delta R)^{1/2} = (1/M_w)^{1/2}(1+q^2R_g^2/6)+2A_2c. \quad (5)$$

Because Eq. (5) cannot be extrapolated to a zero c limit in TR-SLS measurements, calculated M_w is apparent. The contribution of the A_2c term is typically neglected in TR-SLS measurements because it is much smaller than the first term on the right-hand side of Eq. (5).

For *in situ* FT-IR analyses, the measured solutions were mixed in 2 mL polypropylene tubes. Approximately 5 μL of each mixed solution was mounted on the horizontal diamond single crystal of the attenuated total reflection prism of an IR spectrometer (FT-IR; Nicolet 6300, ThermoScientific Co., USA) equipped with a triglycine sulfate (TGS) detector (32 scans, resolution 2 cm^{-1}). The measurement interval was approximately 90 s. The solutions were covered with silicon gum caps to avoid evaporation.

Characterization of the CP phases formed in the solutions containing reference gold nanoparticles and CGNs.

To determine how the material phases, structures and morphologies were altered over time, the CP solutions were sampled at all stages of the reaction (during transformation from the amorphous to the crystalline phase and the subsequent precipitation stage). Aliquots of the solution (~1 mL) were centrifuged for 30 s, and the

materials concentrated at the bottom of the vessel were washed with 2 mL H_2O for approximately 30 s. The washed materials were immediately rewashed with 2 mL a mixed alcoholic solutions (ethanol: isopropanol = 1:1 in volume ratio) several times to remove any residual water and placed in a vacuum vessel.

The materials were observed using TEM, along with analysis of the corresponding selected area electron diffraction (SAED) pattern. Cryo-HR-TEM observations were also performed in order to analyze the structure of the materials at the atomic level. The precipitated samples were also characterized using X-ray diffraction (XRD) analysis, Raman spectroscopy, and nuclear magnetic resonance (NMR) spectroscopy. Details of characterization methods are described in the *Appendix*.

RESULTING DATA

Characterization of the reference gold nanoparticle and CGNs solutions

Fig. 1 plots the results of the dynamic light scattering (DLS) measurements for the reference gold nanoparticle and CGNs solutions. The $G^2(q, t)$ values (Fig. 1a) obtained for the solubilized CGNs at two concentrations were sufficiently resolved (high S/N ratio) to calculate the value for τ. The value of D for each solution was then calculated using Eq. (3) (Fig. 1b), and the concentration dependence was estimated for

235 solutions containing reference gold nanoparticles and CGNs (Figs. 1c and d,
236 respectively). From D_0, the r_H values for the gold nanoparticles and CGNs were
237 calculated as 3.0 ± 0.2 nm and 6.9 ± 0.6 nm, respectively, indicating that -COOH groups
238 were immobilized on the gold nanoparticles. A number-weight analysis was adopted for
239 the calculation of the τ values, causing the errors for r_H in this study to be larger than
240 those seen previously (Onuma et al. 2009) using the same equipment. Note that D
241 increased linearly as the concentration of reference gold nanoparticles increased,
242 suggesting a repulsive intermolecular interaction. Alternatively, the negative
243 relationship between D and the CGNs concentration indicates the existence of an
244 attractive force.

245 The average zeta-potentials of the reference gold nanoparticles and CGNs in the
246 solutions were -45.5 and -48.1 mV, respectively. The visible-light spectra of the
247 reference gold nanoparticles and CGNs in solution were 515.5 nm and 518.5 nm,
248 respectively (Fig. S1 in *Appendix*). These results indicate that the surfaces of the CGNs
249 were more negatively charged than those of the reference gold nanoparticles, due to the
250 ionization of -COOH under the reaction conditions.

251

252 **TR-SLS measurements of the ACP–OCP phase transformation dynamics in**

253 **the reference and CGNs-containing solutions**

254 Using TR-SLS, changes in the M_w and R_g of the CP particles were observed
255 during ACP–OCP phase transformation in the reference gold nanoparticles or
256 CGNs-containing solutions.

257 Fig. 2 plots the changes in M_w, R_g, and the relative density (D_r; M_w/R_g^3) of the CP
258 particles formed in solutions containing 10 μM reference gold nanoparticles or CGNs.
259 The relative density was controlled by the number and rigidity of the particles. The
260 approximate initial M_w and R_g of the particles in the reference solution were 2500 and
261 80 nm, respectively (Figs. 2a and b). Both values rapidly increased during the first 10
262 min, and then continued to gradually increase throughout the next 45 min. After 55 min,
263 however, both values again increased drastically, and the solution became cloudy at ~70
264 min. Conversely, the D_r value (Fig. 2c) remained nearly constant from 10 to 55 min and
265 then rapidly increased thereafter. These results imply that M_w increased from 10 to 55
266 min simply because of particle growth (i.e., an increase in R_g), with no change in the
267 number or rigidity of the particles. After 55 min, however, the increase in M_w was
268 attributed to both an increase in R_g and changes in the number and/or rigidity of the
269 particles, suggesting that phase transformation occurred during this period.

270 The M_w, R_g, and D_r dynamics of CP particles in the CGNs-containing solution

obviously differed from those in the reference gold nanoparticles containing solution. Initially, M_w and R_g in the CGNs-containing solution (approximately 600 and 50 nm, respectively) were much smaller than those in the reference solution (Figs. 2d and e). Throughout the first 10 min, both M_w and R_g rapidly reached local equilibrium values and remained unchanged for 40 min. Between 40 and 50 min, M_w again increased rapidly, reaching a local equilibrium value that was maintained up to 80 min. After 80 min, M_w further increased to a value that was maintained up to 170 min. Note that the value of R_g remained constant from 40 to 170 min. The change in D_r (Fig. 2f) was consistent with that of M_w. Therefore, it can be concluded that the stepwise increases in M_w at 40 and 80 min manifested chiefly from increased particle rigidity (Tsuji et al. 2008). If the number of particles controlled the change in M_w, the sizes of the particles formed in the solution (indicated by the average R_g) should have varied widely. After 170 min, the solution became cloudy, and both M_w and R_g increased drastically. This behavior was observed in both reference and CGNs-containing solutions, although clouding in the CGNs-containing solution was delayed relative to the reference solution by a factor of approximately 3. Following the rapid increase in particle M_w and R_g (after ~70 min and ~170 min in the reference and CGNs-containing solutions, respectively), the solutions became cloudy and precipitates appeared. These initial precipitates were

characterized using XRD and Raman spectroscopy (see below).

During the first 10 min, the value of D_r decreased for both reference and CGNs solutions. Although the reason for this phenomenon remains unclear, it is presumably due to particle aggregation upon increasing size.

TEM analysis of the ACP formed in the reference and CGNs-containing solutions.

The changes in the ACP structure over time prior to the appearance of the initial precipitates in the reference and CGNs-containing solutions were investigated by evaluating the morphologies of the particles using TEM and analyzing their corresponding SAED patterns and lattice fringes. Fig. 3 shows TEM micrographs of the ACP obtained from the reference solution (Fig. 3a-d) and CGNs-containing solution (Fig. 3e-h), along with their corresponding SAED patterns, and cryo-HR-TEM images of their lattice fringes. The solutions were transparent in both cases.

At 10 min, the particles in the reference solution had assembled into a liquid-like form with faint broad Debye rings corresponding to a *d*-spacing of 3.75 Å, (Fig. 3a) which are characteristic of ACP1 (Christoffersen et al. 1990). At 60 min (Fig. 3b), spherical morphology and broad Debye rings of ACP were observed, which are

characteristic of ACP2 (Christoffersen et al. 1990). This result agrees with the TR-SLS analysis, which revealed changes in the internal structure of the ACP during this period (Fig. 2c) (Christoffersen et al. 1990). Cryo-HR-TEM observation showed that, at 60 min, the structure of the ACP in the reference solution was essentially random with uniform contrast to the electron beam and small areas that appeared as black spots ranging from 2 to 10 nm in diameter (Fig. 3c), which is larger than the size of CP clusters (0.7-1.4 nm) (Dey et al. 2010; Onuma and Ito 1998). A magnified cryo-HR-TEM image of these areas is shown in Fig. 4d. They consisted of weak but well-arranged lattice fringes with a *d*-spacing of 3.05 Å. A fast Fourier transform (FFT) image of the lattice fringes showed that the direction of the fringes was constant, which was in stark contrast to that of the lattice fringes of the ACP formed in the CGNs-containing solution (see below).

The morphological evolution of the ACP particles in the CGNs-containing solution essentially matched that of the reference solution. At 10 min, the particles had assembled into a liquid-like form (Fig. 3e). The corresponding SAED pattern showed a halo with no clear rings, indicating ACP1. At 60 min, which was the point when the first local increase in M_w was completed, the ACP morphology was spherical, and a broad Debye ring corresponding to a *d*-spacing of 3.75 Å appeared in the SAED pattern. This pattern typifies ACP2 (Fig. 3f). However, as can be seen in the cryo-HR-TEM images of

the ACP2 particles formed at 60 min in the CGNs-containing solution (Figs. 3g and h), the ACP particles consisted of a major region showing a random-structure (Fig. 3g) and a minor region (<1 % of the observation area) showing complex lattice fringes (Fig. 3h). In addition, in the fringe region, the interspace distance between the neighboring lattice fringes varied from 2.5 to 5.0 Å, and thus it was impossible to identify the actual *d*-spacing. The direction of the lattice fringes was also random. The Ca/P ratios for the ACP in both solutions were ~1.06 at 10 min and then rapidly increased, reaching ~1.25 prior to initial precipitation (~70 min and ~170 min in the reference and CGNs-containing solutions, respectively) (see Fig. S2).

***In situ* FT-IR analysis of the ACP and subsequent precipitates formed in the reference gold nanoparticles or CGNs-containing solutions.**

Fig. 4 shows the *in situ* FT-IR spectra in the P-O stretch region (800–1300 cm^{-1}) of ACP in the initial transparent solutions and the subsequent cloudy solutions with precipitates. Figs. 4a and b correspond to the spectra of the solutions containing the reference gold nanoparticles and CGNs, respectively. The reference solution was transparent until ~70 min, while the CGNs-containing solution was transparent until ~170 min. Immediately after initiating the reaction, intensities of both spectra were too

low to identify; however, ACP particles formed in both solutions as shown by TEM observations. A low-intensity spectrum was observed until 25 min for the reference solution and until 40 min for the CGNs-containing solution. The spectra then showed several specific peaks that gradually evolved, with different peak evolution for each solution.

In the reference solution, the spectrum at 25 min exhibited seven separated peaks at 804, 862, 963, 1024 (with a shoulder at 1034 cm^{-1}), 1049, 1126 and 1189 cm^{-1}. These peaks corresponded to OCP vibrations, with the peak at 963 cm^{-1} attributed to the PO_4^{3-} vibration mode ($\nu_1(PO_4)$) and the remaining peaks attributed mainly to the HPO_4^{2-} ion vibration ($\nu_n(HPO_4)$) or OH^- with HPO_4^{2-} ($\delta_{OH}(HPO_4)$) vibration (Berry and Baddiel 1967). Combined with the XRD data (see section below), we concluded that the initial precipitate in the reference solution was crystalline OCP.

Alternatively, only major CP peaks at 1024 (with a shoulder at 1034 cm^{-1}), and 1126 cm^{-1} appeared in the spectrum of the CGNs-containing solution at 40 min. Note that these peaks corresponding to OCP were clearly seen (broken lines in Figs. 4a and b); however, the peaks at 804, 862, 963, 1049 and 1189 cm^{-1}, which appeared in the reference solution, were not observed in the CGNs-containing solution.

The *in situ* FT-IR spectrum of the initial precipitate in the CGNs-containing solution (after ~170 min) lacked the specific peaks corresponding to OCP HPO_4^{2-} ion vibrations ($\nu_n(HPO_4)$) such as those at 804, 864, 1049, 1105, and 1189 cm^{-1}, which were clearly observed in the spectrum of the precipitate in the reference solution (gray arrows in Fig. 3a). In addition, the spectra of the materials formed in the CGNs-containing solution at all reaction stages lacked the characteristic peak for HAP at 1146 cm^{-1}. These results suggested that CGNs did not induce HAP formation prior to OCP formation under the present reaction conditions. On the basis of this information, combined with the results of the XRD and Raman spectroscopy analyses of the isolated precipitates (see details below), we inferred that the initial precipitate in the CGNs-containing solution is HPO_4-OH-structure-deficient OCP.

XRD, NMR, and Raman analyses of the precipitates formed in the reference and CGNs-containing solutions.

Fig. 5 shows the XRD patterns of the precipitates formed over time taken from the reference solution (a) and CGNs-containing solution (b). The pattern of the initial precipitate taken from the reference solution (at ~70 min after solution preparation) was characteristic of OCP crystals with a (100) peak at 2θ = 4.7°. This XRD pattern was

essentially the same for up to 1 week. Conversely, the XRD pattern of the initial precipitate taken from the CGNs-containing solution (at ~170 min after solution preparation) showed no peak at $2\theta = 4.7°$. Instead, the pattern exhibited a broad peak at around 24°–32°, which corresponded to several CPs; HAP, OCP, and β-TCP (PDF cards 09-0619, 44-0778, and 76-0694, respectively). Therefore, it was not possible to assign this peak to a particular CP. At 12 h after solution preparation, a weak peak corresponding to the (100) orientation of crystalline OCP ($2\theta = 4.7°$) appeared in the XRD pattern of the precipitate taken from the CGNs-containing solution. Notably, the intensity of this peak gradually increased, and the final OCP was also stable for up to at least one week in the CGNs-containing solution. Note that none of the XRD patterns of the materials precipitated from the CGNs-containing solution included the characteristic HAP peak at $2\theta = 10.5°$. However, the intensities of weak peaks corresponding to the (-110) and (010) orientations ($2\theta = 9.2$ and 9.4°, respectively) increased for two days in the CGNs-containing solution, but disappeared at one week. The crystalline OCP structure consists of two HAP-like structures with transition zone and an HPO_4-OH-layer structure between them (see Fig. 8a). The appearance of these two peaks suggested the development of a HAP-like structure with transition zone in OCP (see Fig. 8b). Because the decrease in the intensities of these two peaks corresponded to

396 the development of the conventional OCP structure, we assumed that the precipitated
397 OCP in the CGNs-containing solution had a HAP-like structure with transition zone
398 during the initial precipitation stage, which then transformed to conventional OCP.

399 Fig. 6 presents the ^{31}P solid-state NMR spectra of the initial precipitates taken
400 from the reference solution at ~70 min (initial precipitate), and from CGNs-containing
401 solution at ~170 min (initial precipitate) and two days after starting the reaction. The
402 spectrum of the initial precipitate from the CGNs-containing solution exhibited a broad
403 ^{31}P peak at 3.0 ppm as the main peak, with shoulder at 1.9 and -0.4 ppm. The main peak
404 correspond to the doublet OCP *P1* and *P2/P4* sites of a poorly crystalline nanometric
405 OCP phase, and the shoulder peaks correspond to OCP *P3* (1.9 ppm) and *P5/P6* (-0.4
406 ppm) site, which was confirmed by comparison with the spectrum of initial precipitate
407 (crystalline OCP) from the reference solution shown as dotted spectrum in Fig. 6 (Tsai
408 and Chan 2011). Note that the position of each peak observed in the precipitate from
409 CGNs-containing solution was essentially equivalent to that from the reference solution.
410 The spectrum of the initial precipitate taken from CGNs-containing solution had
411 essentially weak a *P5/P6* peak corresponding to HPO_4^{2-} sites, indicating that the initial
412 precipitate was mainly consisted of PO_4^{3-} rich structures and contained other minor
413 structures corresponding to HPO_4^{2-} structures. The NMR spectra indicated that the

structure of the initial precipitate formed in the CGNs-containing solution was low crystalline OCP, and not HAP.

The spectrum of the precipitate at two days after the reaction exhibited typical OCP peaks at -0.4, 1.9, 3.1, and 3.6 ppm (Tseng et al. 2006; Tsai and Chan 2011) with an additional peak at -1.2 ppm. The presence of the -1.2 ppm peak was evidence that the -COOH altered the HPO_4-OH structure of the OCP lattice through either intercalation or adsorption (Addadi and Weiner 1985; Kamitakahara et al. 2008; Tsai et al. 2010).

Raman spectra of the precipitates from the reference solution (from ~70 min to 1 week) showed similar patterns independent of time (Fig. 7a). Typical OCP peaks at 417, 591 and 961 cm^{-1} and sub-peaks at 609, 1011 and 1048 cm^{-1} were observed. The results of the XRD and Raman analyses of the precipitates taken from the reference solution indicate that OCP was directly formed from ACP without passing through other crystalline intermediate phases.

The time evolution of the Raman spectra of the precipitates taken from the CGNs-containing solution (from ~170 min to one week) is shown in Fig. 7b. All the spectra showed weak peaks attributable to OCP (417, 591, and 961 cm^{-1}) with sub-peaks at 609, and 1048 cm^{-1}. These sub-peaks were also attributed to OCP and their intensities increased over time. However, the intensity of a sub peak at 1011 cm^{-1}, which

corresponded to $\nu_1(HPO_4)$ stretch, of the precipitate formed in the CGNs-containing solution was much weaker at all time points than that of precipitate formed in the reference solution (black arrow in Fig. 7b). Additional broad peaks in the spectra at 170 and 200−300 cm^{-1} were attributed to the glass slide, and were observed in the CGNs-containing solution due to the weaker crystallinity of the precipitates relative to that of the precipitates observed in the reference solution. Consistent with the cryo-HR-TEM observation, the Raman spectra of the precipitates formed in the CGNs-containing solution indicated a HPO_4-OH-deficient OCP structure than that observed for the spectra of the precipitates formed in the reference solution.

The Ca/P ratios of the precipitates from both solutions slowly increased and reached ~1.35 three days after starting the reactions. The precipitates formed in both solutions were observed using TEM (Figs. S3 and S4). Briefly, both initial precipitates were spherical particles (2–5 μm in diameter) consisting of plate-like (reference) or needle-like (CGNs) crystals. In both solutions, the typical OCP plate-like morphology developed at 12 h. Cryo-HR-TEM observation showed the precipitates formed in the CGNs-containing solution consisted almost exclusively of complex lattice fringes, such as those seen in Fig. 4h, which is in contrast to the initial precipitates formed in the reference solution (Fig. S3). Well-arranged lattice fringe regions were also observed,

450 although they were rare (Fig. S4).

451 The *in situ* FT-IR spectra indicated that the ACP formed in the CGNs-containing
452 solution lacked HPO_4^{2-} structures. Consistent with the FT-IR results, the Raman and
453 NMR spectra indicated that the -COOH altered the HPO_4-OH structure of the OCP
454 lattice. In addition, the XRD pattern showed no evidence of HAP in the precipitates
455 (lack of HAP-specific peaks at $2\theta = 10.5°$). We therefore concluded that the materials
456 initially precipitated from the CGNs-containing solution were not conventional OCP,
457 but were OCP-like materials. Furthermore, the results of Raman spectral analyses
458 indicated that the OCP-like material had a HPO_4-OH-layer-deficient structure compared
459 with that of the structure of conventional OCP, and thus was an intermediate phase that
460 appeared during the phase transformation from ACP to OCP. In the CGNs-containing
461 solution, ACP first transformed to HPO_4-OH-layer-deficient OCP, and then converted to
462 conventional OCP over time. However, there were no signs, that CGNs induced HAP
463 formation prior to OCP formation under the present reaction conditions.

464

465 **DISCUSSIONS**

466 The -COOH immobilized on the gold nanoparticles not only delayed the phase
467 transformation from ACP to OCP but also changed the reaction path, resulting in the

formation of an OCP-like intermediate phase. In addition, the results of the cryo-HR-TEM, Raman, and NMR analyses indicated that this OCP-like intermediate phase remained in the final crystalline OCP phase.

Based on the TR-SLS results, the phase transformation from ACP to OCP in the reference solution can be explained as rearrangement of the internal structure from loose (ACP) to rigid (OCP) or as simple nucleation of OCP crystals using ACP as a template. However, the results of the cryo-HR-TEM and *in situ* FT-IR analyses indicated the presence of OCP in the initial ACP, suggesting that the transformation occurred via direct structural rearrangement in the particles. Structural rearrangement of the initial ACP to the final crystalline phase also occurred in the CGNs-containing solution. However, direct rearrangement to OCP was inhibited and an additional intermediate phase (HPO_4-OH-layer-deficient OCP) appeared prior to formation of crystalline OCP. We inferred that CGNs act as a negative catalyst, thus increasing the activation energy of the ACP–OCP phase transformation and inhibiting HPO_4-OH-layer structure evolution. The route involving formation of the HPO_4-OH-structure-deficient OCP phase is a detour that eventually precipitates stable OCP. The final precipitate remained stable for at least 1 week under experimental conditions (Figs. 5 and 7).

The HPO_4-OH-layer-deficient OCP that formed in the CGNs-containing solution

exhibited a structural resemblance to HAP. This similarity might be explained by the formation of Ca-deficient HAP prior to the formation of OCP. The solubility of HAP, even in the Ca-deficient form, is much lower than that of OCP under all pH conditions (Wang and Nancollas 2008). Under high supersaturation conditions, the relatively larger surface energy of HAP (γ_{HAP} = 3.3k_BT, γ_{OCP} = 2.0k_BT) (Onuma et al. 2000; Wu and Nancollas 1997) can be overcome. Ca-deficient HAP could then nucleate before OCP and continue growing until the final reaction stage; although other phases, such as OCP, could coprecipitate during the reaction. However, the characteristic peaks for HAP in the XRD patterns at ~10.5° and the FT-IR spectra (1146 cm^{-1}) for the precipitates formed in the reference and CGNs-containing solutions were not detected at any reaction stage. Therefore, we concluded that the formation of Ca-deficient HAP and subsequent transformation to OCP is unlikely.

The key to the present phase transformation mechanism is the OCP-like structure of the intermediate phase. The OCP unit cell consists of two HAP-like structures with a transition zone weakly linked by an HPO_4-OH-layer. The OCP structure viewed from the *c*-axis is described using an OCP structure profile and VESTA 3 (Brown et al. 1962; Frazier et al. 1991; Momma and Izumi 2011) (Fig. 8a). The HPO_4^{2-} and OH^- vibration bands in the FT-IR and Raman spectra of OCP were mainly attributed to the

504 HPO_4-OH-layer region. Therefore, the lack of these peaks in the FT-IR and Raman
505 spectra of the materials formed in the CGNs-containing solution suggested that this
506 HPO_4-OH layer was deficient. To confirm this hypothesis, the powder diffraction
507 pattern of HPO_4-OH-layer-deficient OCP and HAP were simulated using the
508 RIETAN-FP program (Izumi and Momma 2007), as shown in Fig. 8b. Note that the
509 pattern for the HPO_4-OH-layer-deficient OCP structure lacked the most intense and
510 characteristic peak of OCP at $2\theta = 4.7°$, and thus its structure resembled that of HAP.
511 However, the structure was essentially different from that of crystalline HAP, and thus
512 was referred to as HPO_4-OH-layer-deficient OCP.

513 The ACP–OCP transformation in the CGNs-containing solution is thought to
514 occur as follows. The structure of the initial ACP rearranged to that of the
515 HPO_4-OH-layer-deficient OCP during the initial reaction stage. This structure
516 resembled fragmented HAP, and its XRD pattern lacked the specific OCP diffraction
517 peak at $2\theta = 4.7°$. Next, the HPO_4-OH-layer evolved in the crystalline phase via the
518 so-called maturation process, and OCP with a diffraction peak at $2\theta = 4.7°$ was
519 observed eventually. On the converse, in the reference solution, the transformation
520 proceeded via the direct structural rearrangement of ACP to crystalline OCP. Because
521 this process did not pass through the deficient-structure intermediate phase

522 (HPO_4-OH-layer-deficient OCP), the reaction rate was relatively faster than that of the
523 CGNs-containing solution.
524
525 **IMPLICATIONS**
526 This study has provided new insights into the role of immobilized -COOH in CP
527 mineralization. The observed HPO_4-OH-layer-deficient OCP material is thought to be
528 one of several unknown intermediate phases without typically OCP peak at $2\theta = 4.7°$
529 that form in the presence of appropriate functional groups.
530 This research contributes to our understanding of the complex biomineralization
531 of CPs in the immobilized -COOH rich environments found *in vivo*, including formation
532 processes of dentin and bone involving CPs nucleation on collagen templates and in
533 solutions containing -COOH rich proteins. For example, although the CP crystals of
534 dentine and enamel are both nucleated in the same type of organelles (Kozawa 2009),
535 different crystal structures are formed during subsequent growth stages by the
536 contribution of different type of proteins in the environments. The number of –COOH
537 group in each protein might have some role in this process.
538
539

ACKNOWLEDGMENT

We thank Dr. A. Ito and Dr. Y. Sogo for their help in conducting the XRD analyses, Mr. T. Goto and Mr. D. Fukagawa helping with the TEM observations and TEM sample preparation, Mr. T. Shimada and Ms. A. Tanaka for helping with the visible-light absorption spectroscopy experiments, and Mr. N. Sugimura for his help with the Raman, *in situ* FT-IR, and NMR spectroscopic measurements. This study was partially supported by the Material Characterization Central Laboratory (MCCL) of Waseda University and by a grant-in-aid for Doctoral Course Students (DC2) (number 25-2283) from the Japan Society for the Promotion of Science (JSPS), the Ministry of Education, Culture, Sports, Science and Technology (MEXT), Japan, and by the Nano Processing Facility of the National Institute of Advanced Industrial Science and Technology (AIST).

REFERENCES CITED

Addadi, L., Raz, S., and Weiner, S. (2003) Taking Advantage of Disorder: Amorphous Calcium Carbonate and Its Roles in Biomineralization. Advanced Materials, 12, 959–970.

Addadi, L., and Weiner, S. (1985) Interactions between acidic proteins and crystals: Stereochemical requirements in biomineralization. Proceeding of the National Academy of Science of USA, 82, 4110-4114.

Berry, E.E., and Baddiel, C.E. (1967) Some assignments in the infra-red spectrum of octacalcium phosphate. Spectrochimica Acta, 23A, 1781-1792.

Brown, W.E., Smith, J.P, Lehr, J.R., and Frazier, A.W. (1962) Octacalcium Phosphate and Hydroxyapatite. Nature, 196, 1050–1055.

Christoffersen, M.R., Christoffersen, J., and Kibalczyc, W. (1990) Apparent Solubilities of Two Amorphous Calcium Phosphates and of Octacalcium Phosphate in the Temperature Range 30-42 °C. Journal of Crystal Growth, 106, 349–354.

Davies, E., Muller, K.H., Wong, W.C., Pickard, C.J., Reid, D.G., Skepper, J.N., Duer, M.J. (2014) Citrate bridges between mineral platelets in bone. Proceedings of the National Academy of Science USA, 111, E1354-E1363.

Delgado-Lopez, J.M., Frison, R., Cervellino, A., Gomez-Morales, J., Guagliardi, A.,

576 Masciocchi, N. (2014) Crystal Size, Morphology, and Growth Mechanism in
577 Bio-Inspired Apatite Nanocrystals. Advanced Functional Materials, 24, 1090-1099.
578 Delgado-Lopez, J.M., Iafisco, M., Rodriguez, I., Tampieri, A., Prat, M., Gomez-Morales,
579 J. (2012) Crystallization of bioinspired citrate-functionalized nanoapatite with tailored
580 carbonate content. Acta Biomaterialla, 8, 3491-3499.
581 Dey, A., Bomans, P.H.H., Muller, F.A., Will, J., Frederick, P.M., deWith, G., and
582 Sommerdijk, N.A.J.M. (2010) The Role of Prenucleation Clusters in Surface-Induced
583 Calcium Phosphate Crystallization. Nature Materials, 9, 1010–1014.
584 Falini, G., Albeck, S., Weiner, S., and Addadi, L. (1996) Control of Aragonite or Calcite
585 polymorphism by Mollusk shell Macromolecules. Science, 271, 67–69.
586 Frazier, A.W., Dillard, E.F., Thrasher, R.D., Waerstad, K.R., Hunter, S.R., Kohler,
587 J.J., Scheib, R.M. (1991) Crystallographic properties of Fertilizer Compounds
588 TVA/NFERC-91/4; TVA-Bull-Y-217 ON: DE93003931, National Fertilizer and
589 Environmental Research Center, Muscle Shoals, AL, USA.
590 Gebauer, D., Völkel, A., and Cölfen, H. (2008) Stable Prenucleation Calcium Carbonate
591 Clusters. Science, 322, 1819–1822.
592 Hamm, L.M., Giuffre, A.J., Han, M., Tao, J., Wang, D., DeYoreo, J.J., and Dove, P.M.
593 (2014) Reconciling Disparate Views of Template-Directed Nucleation through

Measurement of Calcite Nucleation Kinetics and Binding Energies. Proceedings of the National Academy of Science of USA, 111, 1304–1309.

He, G., Dahl, T., Veis, A., and George, A. (2003) Nucleation of Apatite Crystals in vitro by Self-Assembled Dentin Matrix Protein 1. Nature Materials, 2, 552–558.

Hu, Y.Y., Rawal, A. and Schmidt-Rohr, K. (2010) Strongly bound citrate stabilizes the apatite nanocrystals in bone. Proceedings of the National Academy Science of USA, 107, 22425-22429.

Iijima, M., Tohda, H., and Moriwaki, Y. (1992) Growth and Structure of Lamellar Mixed Crystals of Octacalcium Phosphate and Apatite in a Model System of Enamel Formation. Journal of Crystal Growth, 116, 319–326.

Izumi, F. and Momma, K. (2007) Three-dimensional visualization in powder diffraction. Solid State Phenomenon, 130, 15-20.

Kamitakahara, M., Okano, H., Tanihara, M., and Ohtsuki, C. (2008) Synthesis of octacalcium phosphate intercalated with dicarboxylate ions from calcium carbonate and phosphoric acid. Journal of the Ceramic Society of Japan, 116, 481-485.

Kanzaki, N., Treboux, G., Onuma, K., Tsutsumi, S., and Ito, A. (2001) Calcium phosphate clusters. Biomaterials, 22, 2921–2929.

Kanzaki, N., Uyeda, Q.P.T., and Onuma, K. (2006) Intermolecular interaction of actin

612 revealed by a dynamic light scattering technique. Journal of Physical Chemistry B, 110,
613 2881–2887.
614 Kozawa, Y. (2009) Chapter 4: Enamel structure and amelogenesis, Tooth Enamel
615 -Development, Structure, Gene, Tissue Engineering, Origin and Evolution. pp.187-223,
616 Wakaba Publishing Ltd., Tokyo, Japan.
617 Lehner, D., Kellner, G., Schnablegger, H., and Glatter, O. (1998) Static Light Scattering
618 on Dense Colloidal Systems: New Instrumentation and Experimental Results. Journal of
619 Colloid Interface Science, 201, 34–47.
620 Mann, S. (2001) Biomineralization Principles and Concepts in Bioinorganic Materials
621 Chemistry; Oxford University Press, U.K.
622 Momma, K. and Izumi, F. (2011) VESTA 3 for three-dimensional visualization of
623 crystal, volumetric and morphology data. Journal of Applied Crystallography, 44,
624 1272-1276.
625 Nelson, D.G.A., Barry, J.C., Shields, S.C.P., Glena, R., and Featherstone, J.D.B. (1989)
626 Crystal Morphology Composition, and Dissolution Behavior of Carbonate Apatites
627 Prepared at Controlled pH and Temperature. Journal of Colloid and Interface Science,
628 130, 467–479.
629 Nonoyama, T., Kinoshita, T., Higuchi, M., Nagata, K., Tanaka, M., Sato, S., and Kato, K.

630 (2011) Multistep Growth Mechanism of Calcium Phosphate in the Earliest Stage of
631 Morphology-Controlled Biomineralization. Langmuir, 27, 7077–7083.
632 Nudelman, F., Lausch, A.J., Sommerdijk, N.A.J.M., and Sone, E.D. (2013) In vitro
633 Models of Collagen Biomineralization. Journal of Structural Biology, 183, 258–269.
634 Nylen, M.U., Eanes, E.D., and Omnel, K.A. (1963) Crystal Growth in Rat Enamel.
635 Journal of Cell Biology, 18, 109–123.
636 Onuma, K., Furubayashi, N., Shibata, F., Kobayashi, Y., Kaito, S., Ohnishi, Y., and
637 Inaka, K. (2009) Anomalous effect of poly(ethylene)glycol on intermolecular
638 interaction and protein association. Crystal Growth Design, 9, 2517–2524.
639 Onuma, K., and Ito, A. (1998) Cluster Growth Model for Hydroxyapatite. Chemistry of
640 Materials, 10, 3346–3351.
641 Onuma, K., Kanzaki, N., Ito, A., and Tateishi, T. (1998) Growth Kinetics of the
642 Hydroxyapatite (0001) Face Revealed by Phase Shift Interferometry and Atomic Force
643 Microscopy. Journal of Physical Chemistry B 102, 7833-7838.
644 Onuma, K., Oyane, A., Tsutsui, K., Tanaka, K., Treboux, G., Kanzaki, N., and Ito, A.
645 (2000) Precipitation Kinetics of Hydroxyapatite Revealed by the Continuous-Angle
646 Laser Light Light-Scattering Technique. Journal of Physical Chemistry B 104,
647 10563–10568.

Posner, A.S., and Betts, F. (1975) Synthetic Amorphous Calcium Phosphate and its Relation to Bone Mineral Structure. Accounting of Chemistry Research, 8, 273–281.

Powder Diffraction File (PDF) Card. No. 09-0169.

Powder Diffraction File (PDF) Card. No. 44-0778.

Powder Diffraction File (PDF) Card. No. 76-0694.

Provencher, S.W. (1982) Users Manual for CONTIN, Technical Report EMBL-DAO5, Queens University Belfast, UK.

Sunagawa, I. (2005) Crystals Growth, Morphology and Perfection; Cambridge University Press, U.K.

Tsai, T.W.T. and Chan, J.C.C. (2011) Chapter 1: Recent Progress in the Solid-State NMR Studies of Biomineralization, Annual Reports on NMR Spectroscopy, Volume 73, pp.1-61, Elsevier Ltd., the Netherland.

Tsai, T.W.T., Chou, F., Tseng, Y., Chan, J.C.C. (2010) Solid-state P-31 NMR study of octacalcium phosphate incorporated with succinate. Physical Chemistry Chemical Physics, 12, 6692-6697.

Tseng, Y., Fedorov, E., McCaffery, J.M., Almo, S.C., and Wirtz, D. (2001) Micromechanics and Ultrastructure of Actin Filament Networks Crosslinked by Human Fascin: A Comparison with α-Actinin. Journal of Molecular Biology, 310, 351–366.

666 Tseng, Y., Mou, C., and Chan, J.C.C. (2006) Solid-State NMR Study of the
667 Transformation of Octacalcium Phosphate to Hydroxyapatite: A Mechanistic Model
668 for Central Dark Line Formation. Journal of the American Chemical Society, 128,
669 6909-6918.

670 Tsuji, T., Onuma, K., Yamamoto, A., Iijima, M., and Shiba, K. (2008) Direct
671 Transformation from Amorphous to Crystalline Calcium Phosphate Facilitated by
672 Motif-Programmed Artificial Proteins. Proceedings of the National Academy of Science
673 of USA, 105, 16866–16870.

674 Veis, A. (2003) Mineralization in Organic Matrix Frameworks. P.M. Dove, J.J. DeYoreo,
675 and S. Weiner (Eds.), Biomineralization, Reviews in Mineralogy and Geochemistry Vol.
676 54. pp. 249–289. Mineralogical Society of America, Chantilly Virginia, USA.

677 Wang, C.G., Liao, J.W., Gou, B.D., Huang, J., Tang, R.K., Tao, J.H., Zhang, T.L., and
678 Wang, K. (2009) Crystallization at Multiple Sites inside Particles of Amorphous
679 Calcium Phosphate. Crystal Growth Design, 9, 2620–2626.

680 Wang, L., and Nancollas, G.H. (2008) Calcium Orthophosphates: Crystallization and
681 Dissolution. Chemical Review, 108, 4628–4669.

682 Weiner, S., and Dove, P.M. (2003) An Overview of Biomineralization Processes and the
683 Problem of the Vital Effect. P.M. Dove, J.J. DeYoreo, and S. Weiner (Eds.),

684 Biomineralization, Reviews in Mineralogy and Geochemistry Vol. 54. pp. 1–30.
685 Mineralogical Society of America, Chantilly Virginia, USA.
686 Xie, B.Q. and Nancollas, G.H. (2010) How to control the size and morphology of
687 apatite nanocrystals in bone. Proceeding of the National Academy of Science of USA,
688 107, 22369-22370.
689 Wu, W., and Nancollas, G.H. (1997) Nucleation and Crystal Growth of Octacalcium
690 Phosphate on Titanium Oxide Surfaces. Langmuir 13, 861-865.
691 Zhao, J., Liu, Y., Sun, W., and Yang, X. (2012) First Detection, Characterization, and
692 Application of Amorphous Calcium Phosphate in Dentistry. Journal of Dental Science,
693 7, 316–323.
694
695
696
697
698
699
700
701

Figure Captions

FIGURE 1. DLS measurements of the reference gold nanoparticles and CGNs-containing solutions. (**a**) Second autocorrelation functions at θ = 30° (solid gray line) and 90° (broken gray line) for the solution containing 150 μM CGNs and at θ = 30° (solid black line) and 90° (broken black line) for the solution containing 37.5 μM CGNs. (**b**) Relation between $1/\tau$ and q^2 for the solutions containing 60 μM reference gold nanoparticles (black diamonds) and 120 μM CGNs (grey circles). (**c**) Relation between D and the concentration of reference gold nanoparticles. (**d**) Relation between D and the CGNs concentration.

FIGURE 2. TR-SLS analysis results for the solutions containing 10 μM reference gold nanoparticles (top panels; (**a**)–(**c**)) and 10 μM CGNs (bottom panels; (**d**)–(**f**)). Shown are the temporal changes in the apparent M_w (left), R_g (center), and D_r (right) of the particles in solution.

FIGURE 3. TEM micrographs with SAED patterns (inset) and FFT images of the ACP formed in the reference (200 kV) and CGNs-containing solutions (300 kV). (**a**) Liquid-like ACP in the reference solution at 10 min. (**b**) Spherical ACP in the reference

720 solution formed at 60 min. (**c**) Cryo-HR-TEM micrograph of the ACP in the reference
721 solution formed at 60 min. Black dots ranging from 2–10 nm can be seen. (**d**)
722 Cryo-HR-TEM micrograph of the dots in (**c**) with the corresponding FFT image. (**e**)
723 Liquid-like ACP formed at 10 min in the CGNs-containing solution. (**f**) Spherical ACP
724 formed at 60 min in the CGNs-containing solution. All times correspond to those after
725 solution preparation. (**g**) Cryo-HR-TEM micrograph of the completely random structure
726 of the ACP in formed at 60 min in the CGNs-containing solution with the corresponding
727 FFT image. (**h**) Cryo-HR-TEM micrograph of the ACP with the corresponding FFT
728 image in the CGNs-containing solution at 60 min. Complex lattice fringes are observed.
729
730 **FIGURE 4.** *In situ* FT-IR spectra of ACP in the reference (**a**) and CGNs-containing
731 (**b**) solutions at various reaction stages. Broken black lines indicate typical OCP peaks:
732 963, 1021 and 1124 cm^{-1}. Broken gray arrows indicate OCP peaks that disappear in the
733 ACP and precipitate formed in the CGNs-containing solution.
734
735 **FIGURE 5.** Time evolution of the XRD patterns of the precipitates taken from the (**a**)
736 reference solution and (**b**) CGNs-containing solution. The solid black circles correspond
737 to the OCP peaks.

738

739 **FIGURE 6.** Solid-state ^{31}P NMR spectra of (**a**) the initial precipitate from the reference
740 solution (broken gray line) and (**b**) the initial precipitate and material (**c**) after two day
741 from CGNs-containing solution (black solid line). Black arrows indicate the OCP peaks.
742 Gray arrow indicates the -COOH containing OCP peak (P_A and P_B: Tsai et al. 2010).

743

744 **FIGURE 7.** Time evolution of the Raman spectra of the precipitates taken from the (**a**)
745 reference solutions and (**b**) CGNs-containing solutions. The solid black circles
746 correspond to the OCP peaks. The black arrow in (**b**) indicates a peak at 1011 cm^{-1}
747 corresponding to $v_1(HPO_4)$ stretch.

748

749 **FIGURE 8.** (**a**) Crystal structures of OCP, HPO_4-OH-layer-deficient OCP, and HAP
750 viewed from the *c*-axis. (**b**) Simulated powder diffraction patterns of OCP, HPO_4-OH
751 layer deficient OCP, and HAP.

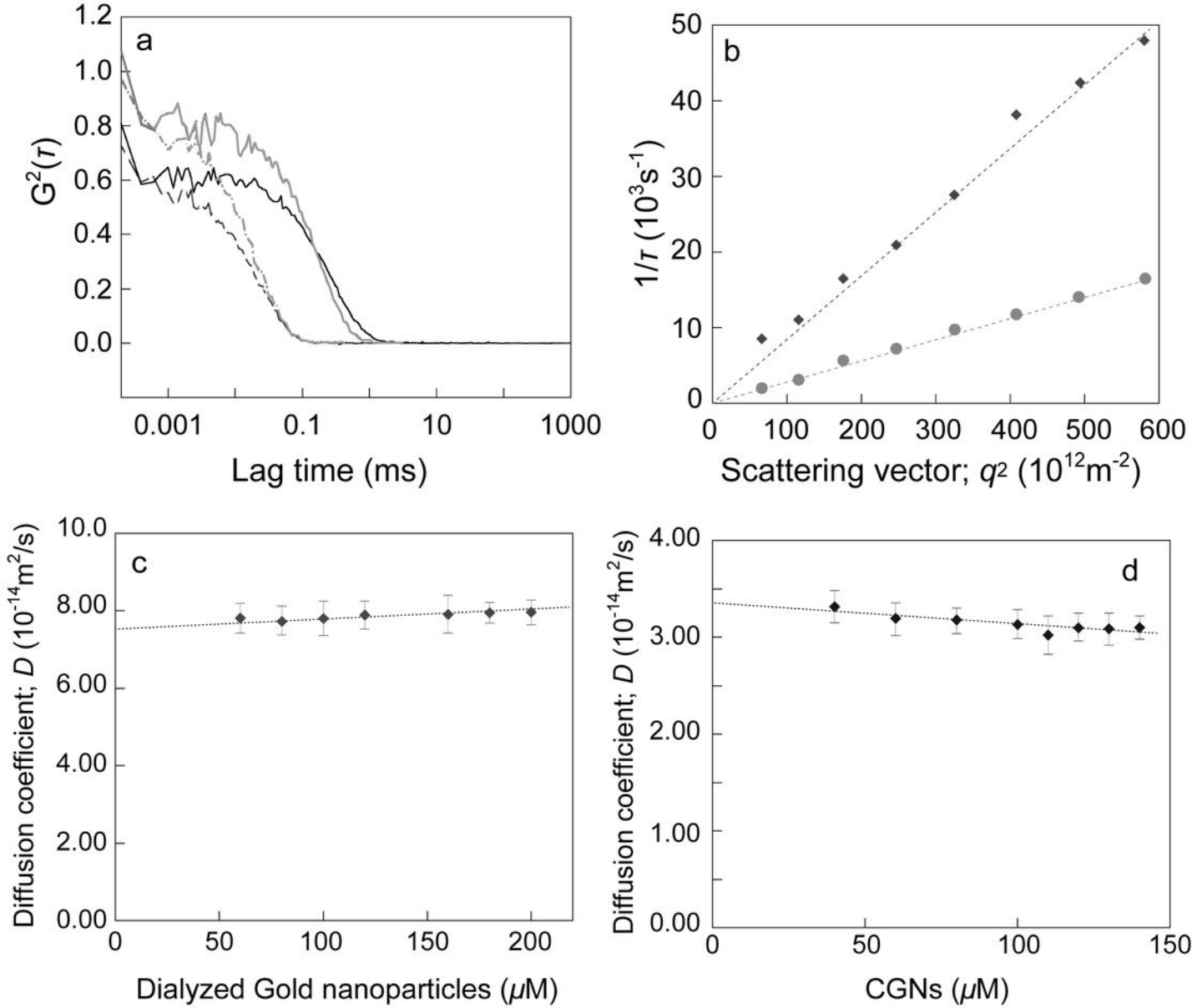
a
$G^2(\tau)$
1.2
1.0
0.8
0.6
0.4
0.2
0.0
0.001
0.1
10
1000
Lag time (ms)
b
$1/\tau$ ($10^3 s^{-1}$)
50
40
30
20
10
0
0
100
200
300
400
500
600
Scattering vector; q^2 ($10^{12} m^{-2}$)
c
Diffusion coefficient; D ($10^{-14} m^2/s$)
10.0
8.00
6.00
4.00
2.00
0.00
0
50
100
150
200
Dialyzed Gold nanoparticles (μM)
d
Diffusion coefficient; D ($10^{-14} m^2/s$)
4.00
3.00
2.00
1.00
0.00
0
50
100
150
CGNs (μM)

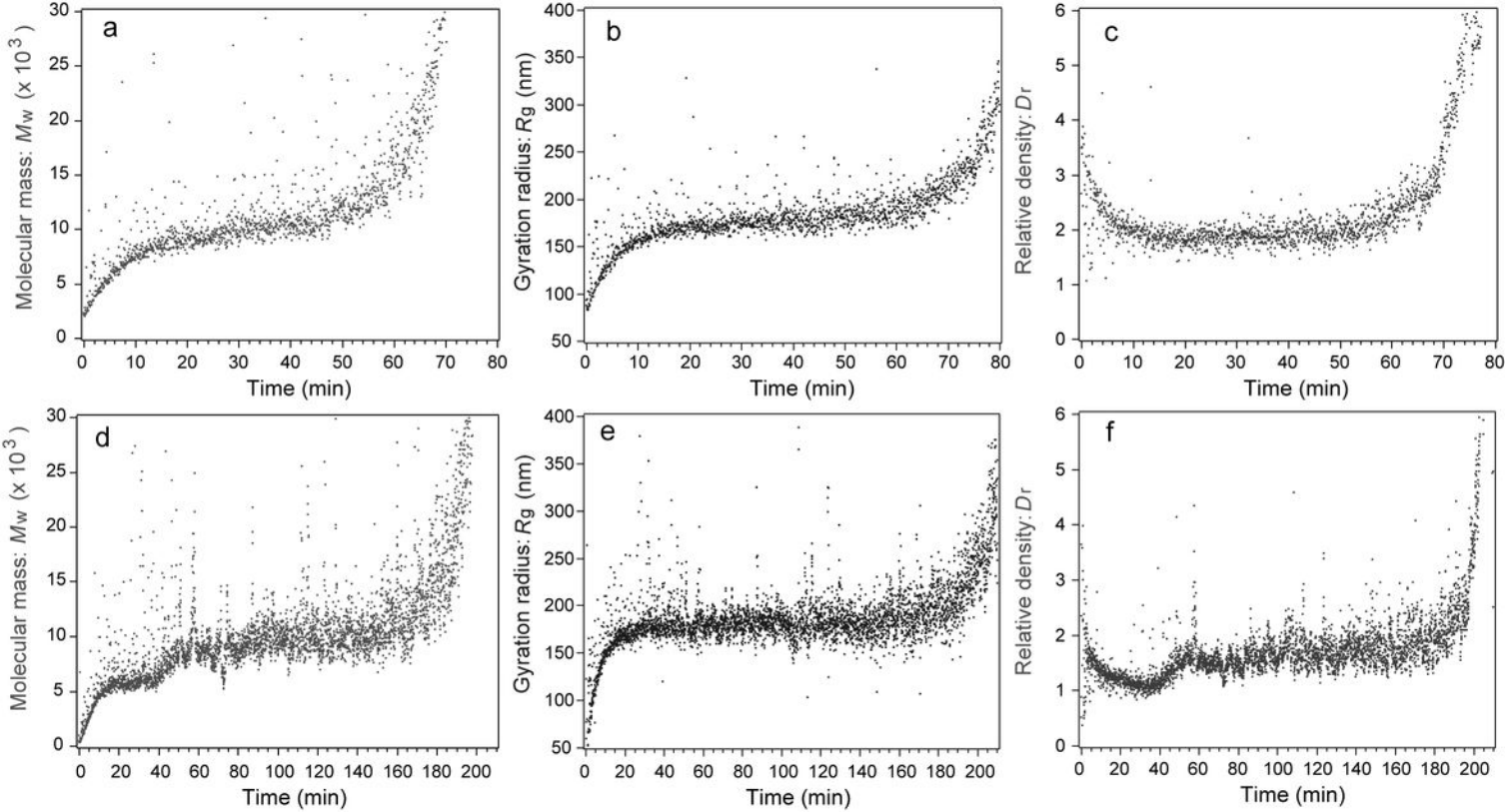
a
b
c
d
e
f
Molecular mass: M_w (x 10^3)
Gyration radius: R_g (nm)
Relative density: D_r
Time (min)

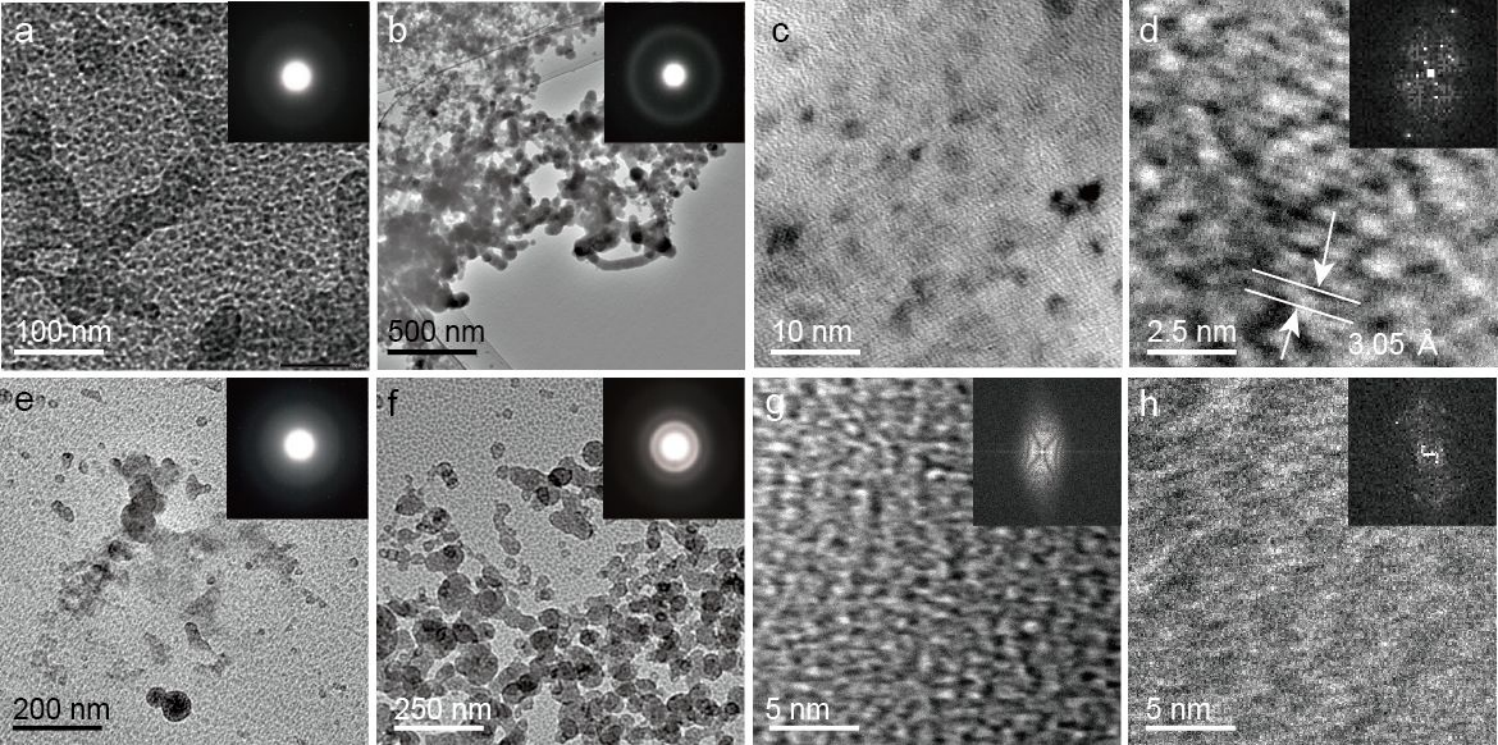
a
100 nm
b
500 nm
c
10 nm
d
2.5 nm
3.05 Å
e
200 nm
f
250 nm
g
5 nm
h
5 nm

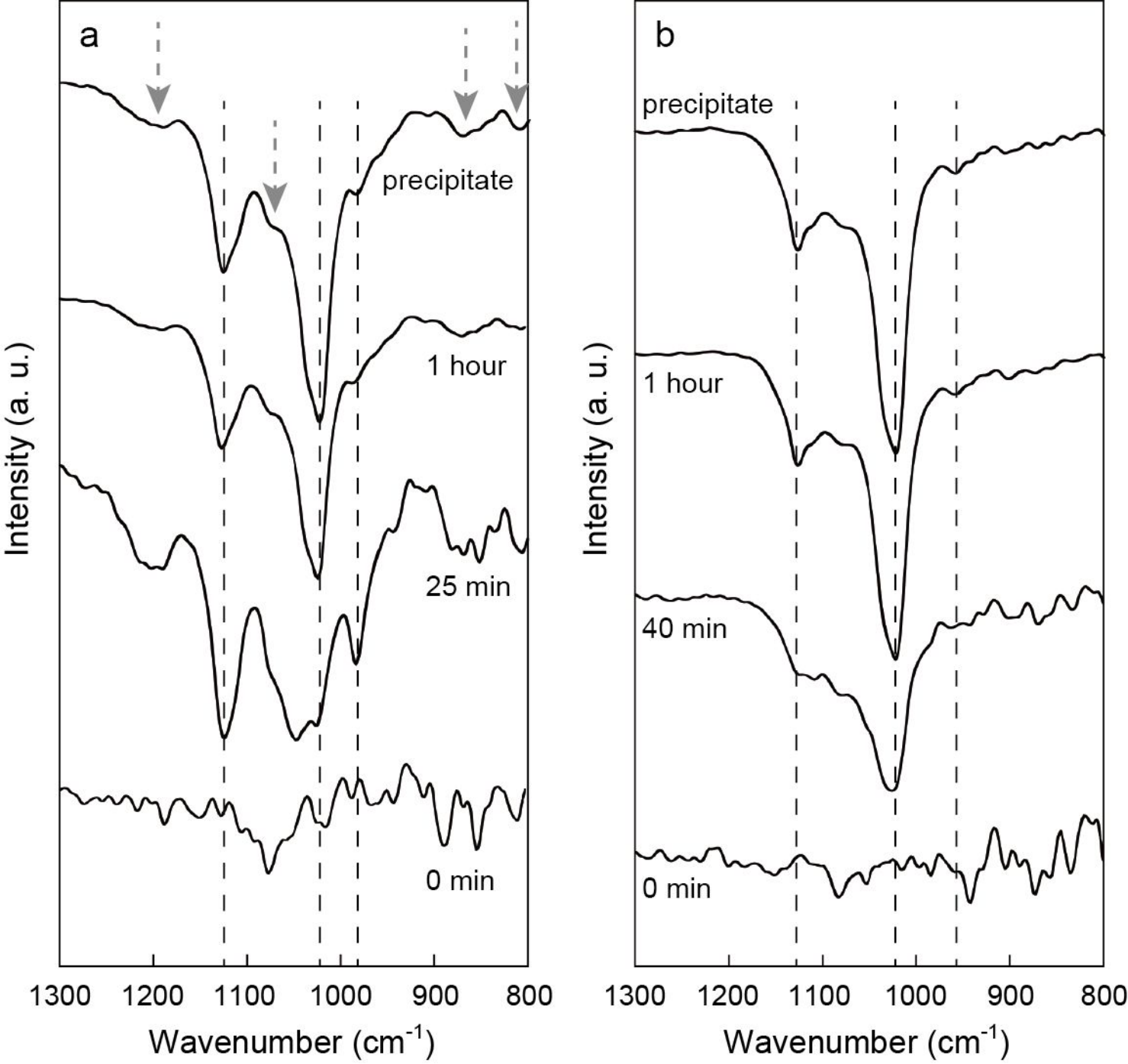
a
precipitate
1 hour
25 min
0 min
Intensity (a. u.)
1300
1200
1100
1000
900
800
Wavenumber (cm-1)
b
precipitate
1 hour
40 min
0 min
Intensity (a. u.)
1300
1200
1100
1000
900
800
Wavenumber (cm-1)

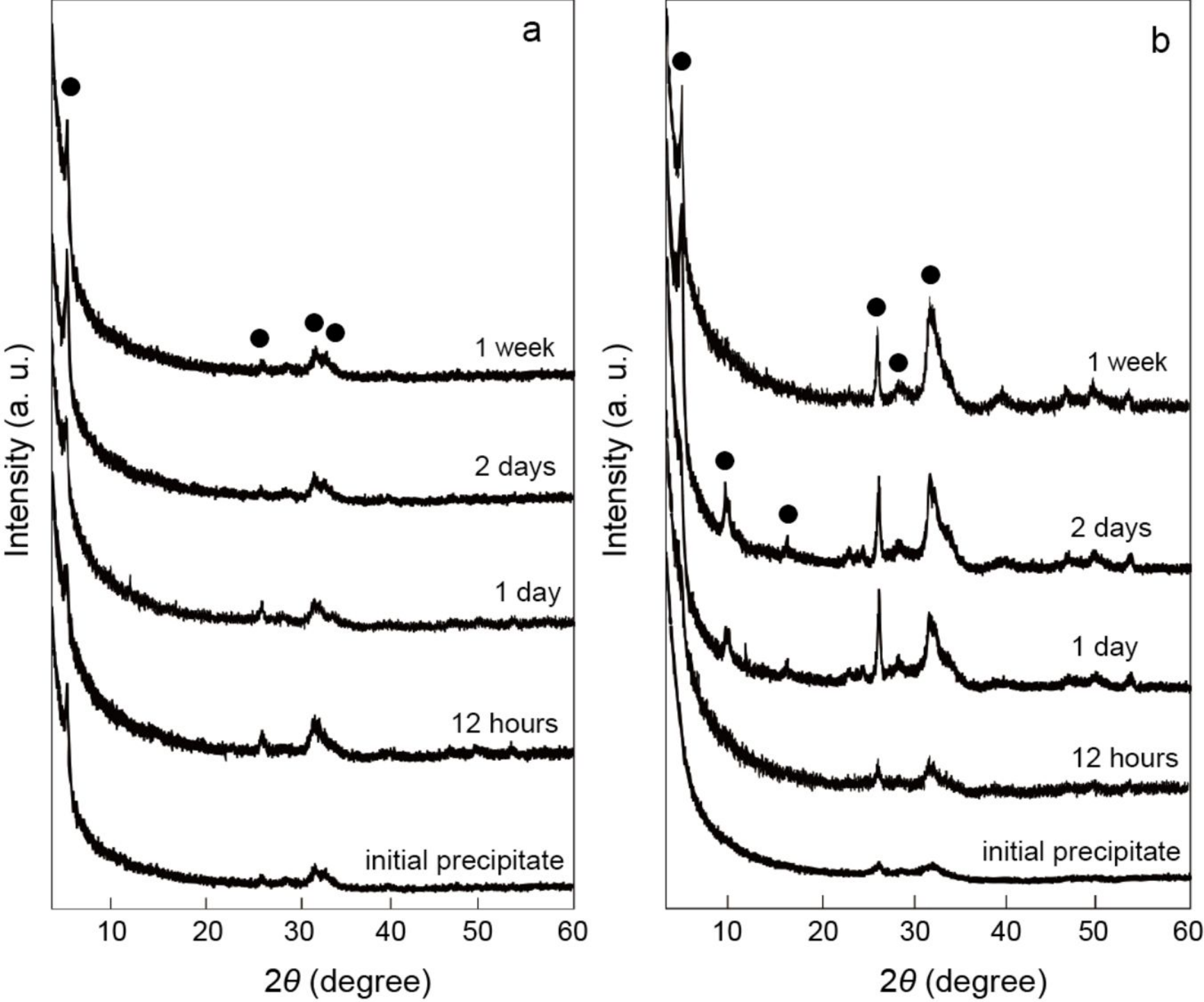
a
b
1 week
2 days
1 day
12 hours
initial precipitate
Intensity (a. u.)
2θ (degree)
10
20
30
40
50
60

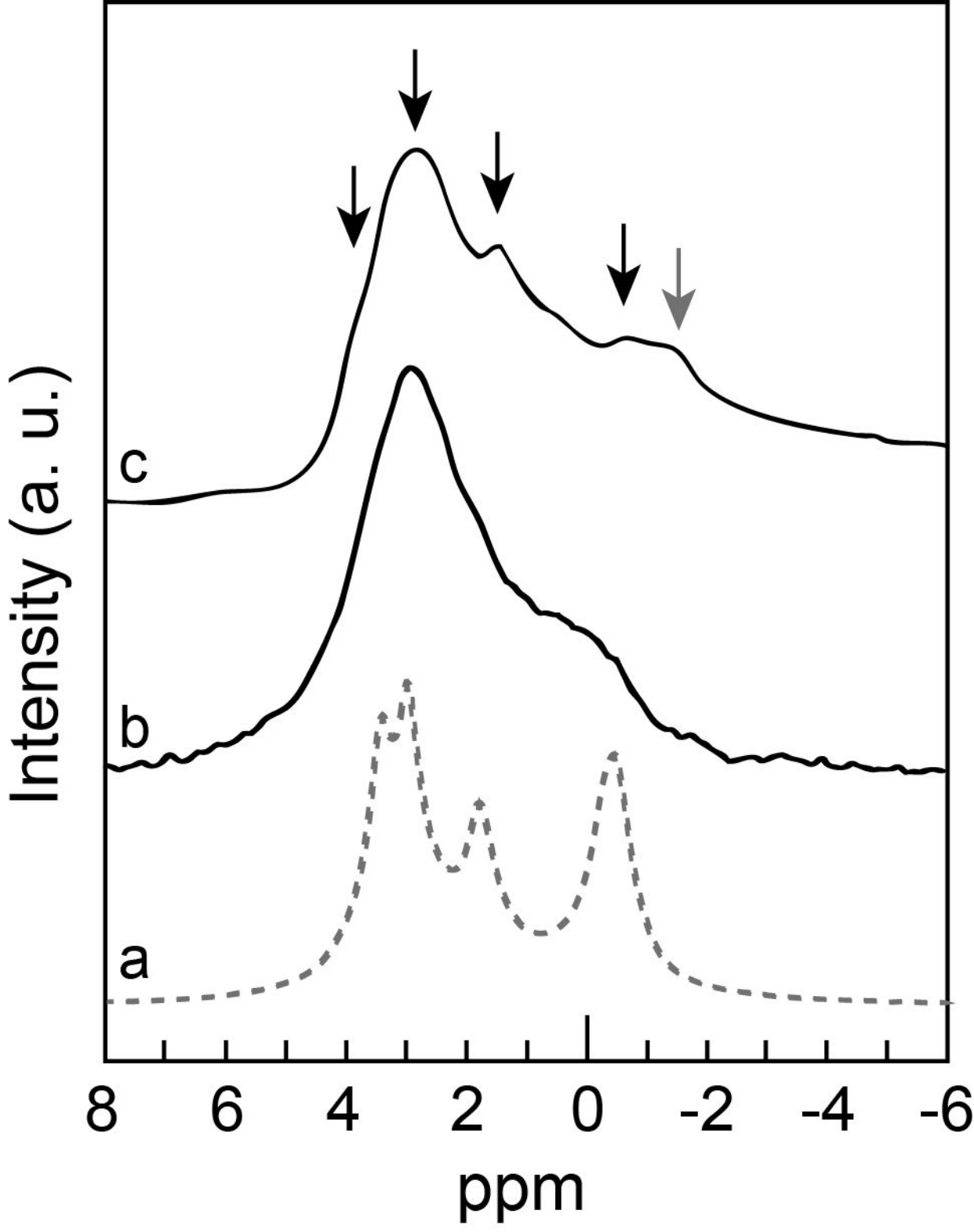
Intensity (a. u.)
c
b
a
8
6
4
2
0
-2
-4
-6
ppm

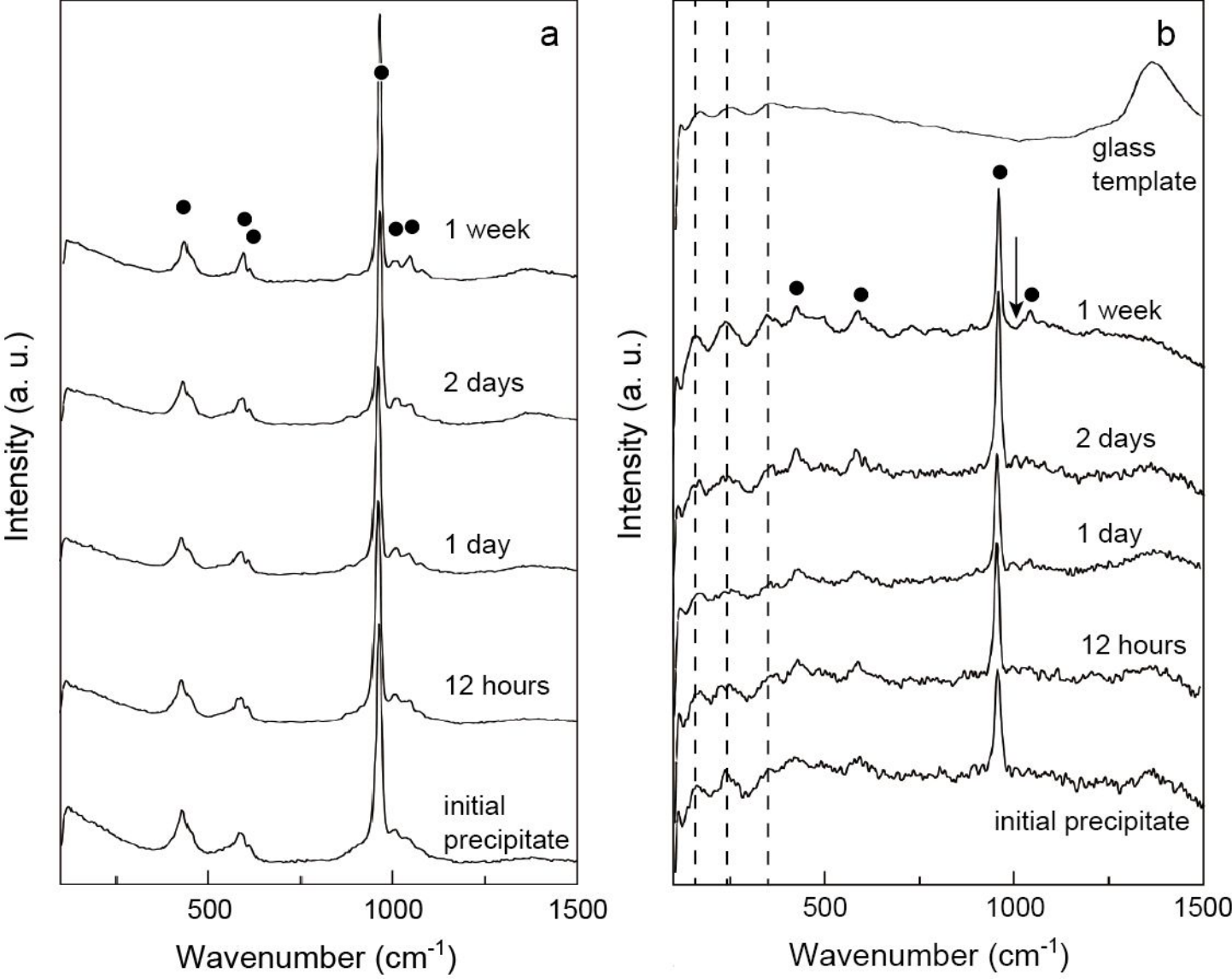
a
1 week
2 days
1 day
12 hours
initial
precipitate
Intensity (a. u.)
500
1000
1500
Wavenumber (cm-1)
b
glass
template
1 week
2 days
1 day
12 hours
initial precipitate
Intensity (a. u.)
500
1000
1500
Wavenumber (cm-1)

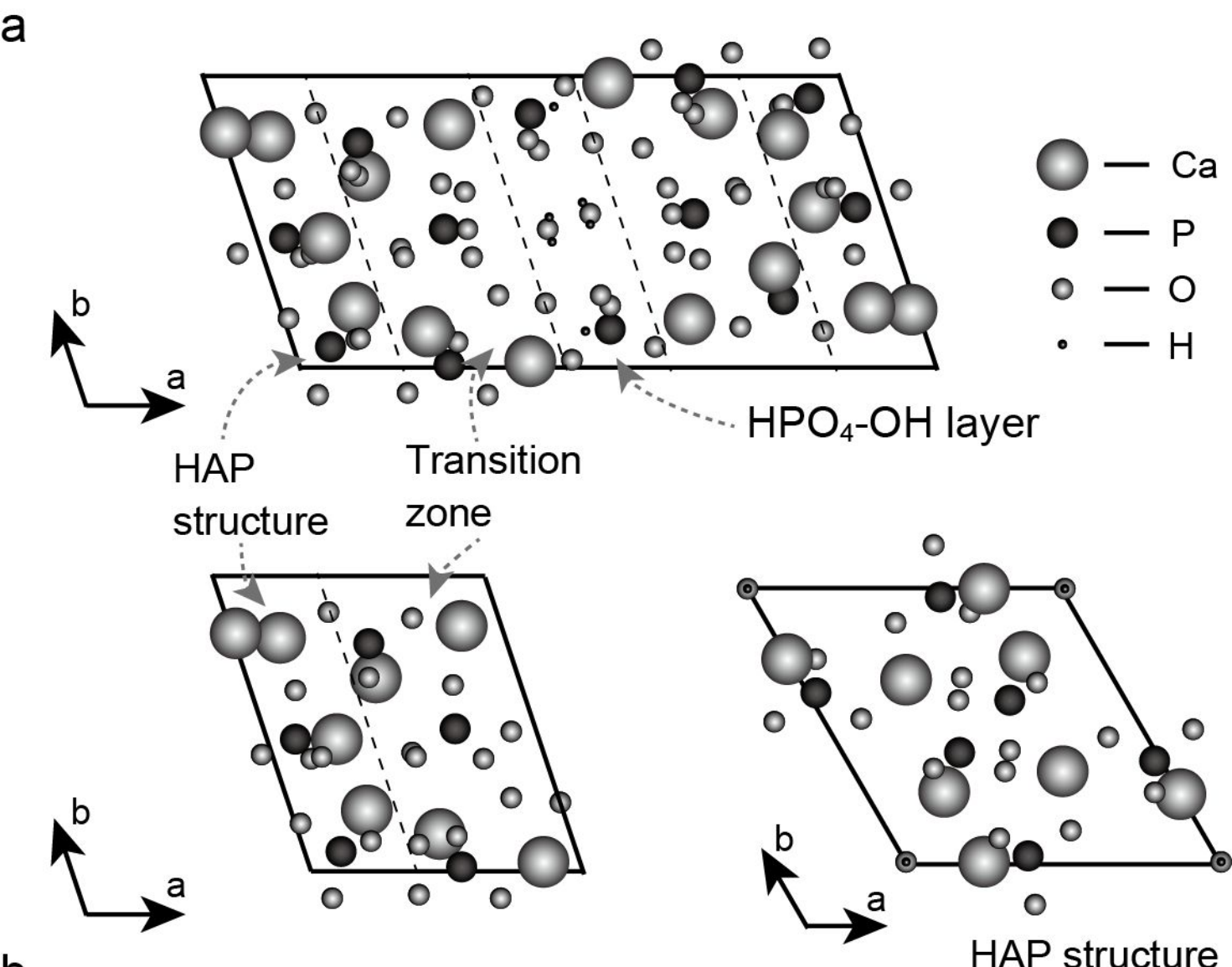
a
Ca
P
O
H
b
a
HPO4-OH layer
HAP
structure
Transition
zone
b
a
b
a
HAP structure

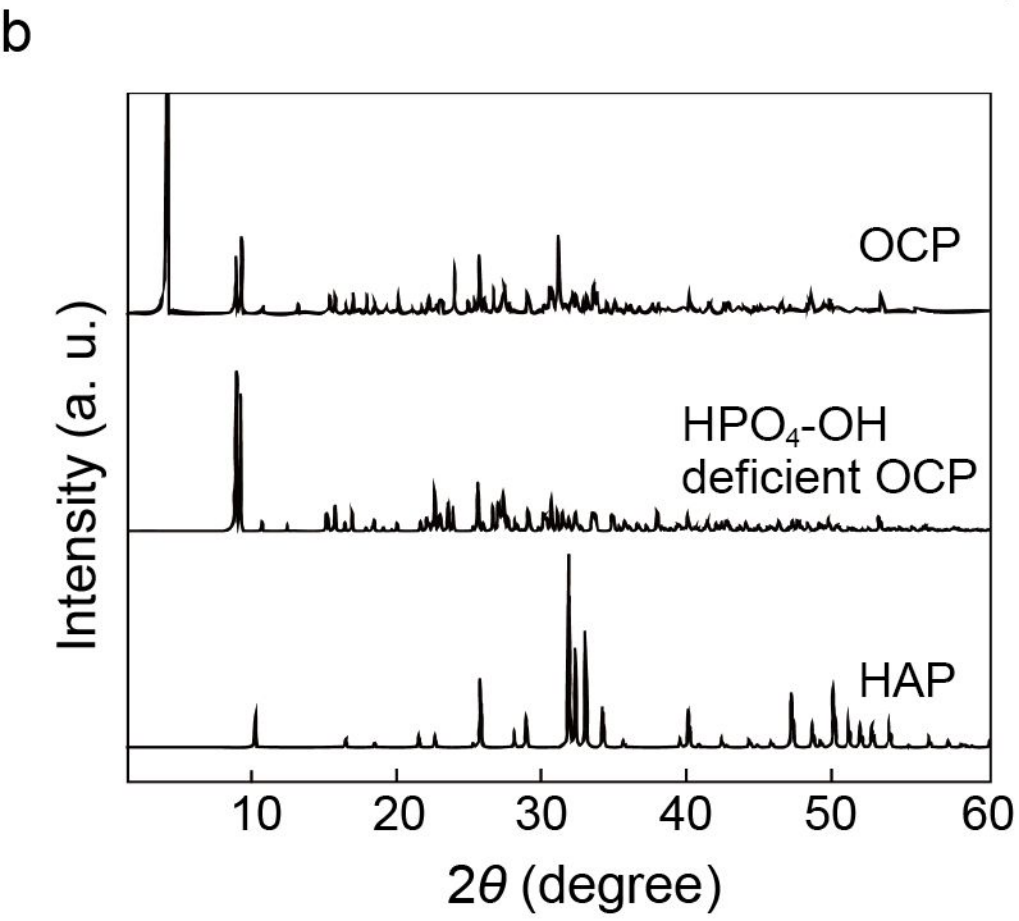
b
OCP
HPO4-OH
deficient OCP
HAP
Intensity (a. u.)
10
20
30
40
50
60
2θ (degree)